Luminescence chronology of fossiliferous fluvial sediments along the middle Atbara River, Sudan

Sumiko Tsukamoto, Robert Bussert, Anne Delagnes, Marcus Richter, Mosab Mohammednoor, O. Bedri, Brian Kraatz, Johannes Müller, Khalafallah Salih, Ali Eisawi, et al.

Quaternary Geochronology 71 (2022) 101312

Contents lists available at ScienceDirect

Quaternary Geochronology

journal homepage: www.elsevier.com/locate/quageo

Luminescence chronology of fossiliferous fluvial sediments along the middle Atbara River, Sudan

S. Tsukamoto [a,*], R. Bussert [b], A. Delagnes [c], M. Richter [a], M. Mohammednoor [b,d,e], O. Bedri [f], B. Kraatz [g], J. Müller [d], K. Salih [h], A. Eisawi [e,h], F. Bibi [d]

[a] Leibniz Institute for Applied Geophysics, Hannover, Germany
[b] Technische Universität Berlin, Germany
[c] PACEA, CNRS/Université de Bordeaux, Allée Geoffroy Saint-Hilaire, Pessac CEDEX, France
[d] Museum für Naturkunde, Leibniz Institute for Evolution and Biodiversity Science, Berlin, Germany
[e] University of Khartoum, Sudan
[f] International University of Africa, Khartoum, Sudan
[g] Western University of Health Sciences, Pomona, USA
[h] Al Neelain University, Khartoum, Sudan

ARTICLE INFO

Keywords:
Luminescence dating
Feldspar pulsed IRSL
Quartz OSL
Fluvial sediments
Atbara river
Pleistocene

ABSTRACT

Fluvial sediments of the middle Atbara River Valley, eastern Sudan, contain abundant vertebrate fossils and stone tools. Previous work described two sedimentary units, the Butana Bridge Synthem (BBS) and the Khashm El Girba Synthem (KGS), with three divisions each (BBS1-3 and KGS1-3, from bottom to top, respectively). ^{230}Th/U dating on bivalve shells suggested an age of ~126 and ~92 ka for the basal KGS2 and basal KGS3, respectively, and mammalian biochronology in combination with magnetostratigraphy suggested an age of late Early to early Middle Pleistocene for the underlying BBS. To establish a detailed chronology of this fluvial sedimentary sequence, we collected 17 luminescence samples from both sides of the Atbara River close to the Butana Bridge. Quartz OSL dating was applied to samples from the upper part of the profile (upper KGS2 and KGS3), but the signal reached saturation within the upper ~10 m of the sequence. To select a suitable feldspar signal to date older samples beyond the limit of the quartz OSL, a comparison of the quartz OSL, feldspar post-IR IRSL at 225 and 290 °C, and pulsed IRSL signal at 50 °C was conducted for a sample from KGS3. The result showed that only the fading corrected pulsed IRSL yielded an age consistent with the quartz OSL, and the post-IR IRSL signals (both at 225 and 290 °C) overestimated the quartz age significantly. We therefore selected the pulsed IRSL signal to date the older deposits. The luminescence ages indicate that the entire BBS - KGS sequence was deposited between 224 ± 23 ka and <17 ± 1 ka, corresponding to marine isotope stages (MIS) 7–2, significantly revising previous conclusions.

1. Introduction

The Atbara River is one of the major tributaries of the Nile in eastern Sudan, originating from the Ethiopian Highlands (Fig. 1a). Its middle to lower reaches comprise a narrow fluvial valley located between the Red Sea Hills to the east and the Butana Desert to the west (Fig. 1b), with up to 50 m thick fluvial sediments deposited on Cenozoic basalts, Cretaceous sandstones, or even older basement rocks. These fluvial sediments contain vertebrate fossils and stone artefacts (Arkell, 1949; Abbate et al., 2010), which indicate favourable environments existed for diverse large mammals including hominins, although little investigation has been made in this region compared to contemporaneous sites in the nearby East African Rift Valley (e.g. Clark et al., 2003; Potts et al., 2018).

The Pleistocene strata of the middle Atbara were described in detail by Abbate et al. (2010). They divided the fluvial sequence into the lower Butana Bridge Synthem (BBS) and the upper Khashm El Girba Synthem (KGS), which they separated by a major unconformity. The BBS was divided into three 'intervals' (BBS1-3) and the KGS into three subsynthems (KGS1-3) separated by minor unconformities. ^{230}Th/U dating of *Etheria* shells in channel fill sediments marking the bases of the KGS2 and KGS3 gave ages of 126.1 ± 1.0 ka and 92.2 ± 0.7 ka, respectively (Abbate et al., 2010). Deposition of the KGS1 was correlated with the

* Corresponding author.
E-mail address: Sumiko.Tsukamoto@leibniz-liag.de (S. Tsukamoto).

https://doi.org/10.1016/j.quageo.2022.101312
Received 1 December 2021; Received in revised form 8 April 2022; Accepted 13 April 2022
Available online 29 April 2022

marine isotope stage (MIS)7 (243–191 ka; Lisiecki and Raymo, 2005), while the KGS2 and KGS3 were correlated with MIS5 (130–71 ka; Lisiecki and Raymo, 2005). No numerical chronology was obtained for the BBS, but the age of the BBS1 was suggested to be Early Pleistocene based on mammal biochronology, particularly based on the presence of *Hippopotamus* cf. *gorgops* and *Elephas recki recki*. Five normal-polarity palaeomagnetic samples from the BBS2 interval were assigned to the Brunhes Chron, and therefore earliest Middle Pleistocene, while the well-developed calcretes of the BBS2 and BBS3 were interpreted as having spanned most of the Middle Pleistocene. Therefore, the overall evidence suggested a late Early to early Middle Pleistocene age for the entire BBS, with the unconformity between the BBS and KGS synthems proposed to be around 100 kyr in duration. Deposition of the basal BBS was also proposed to coincide with a humid interval (Abbate et al., 2010).

Beginning in 2018, we restarted work in this underexplored area and made new palaeontological, sedimentological, and archaeological discoveries. A major focus of the current expedition has been the improvement of geochronological control for the middle Atbara sediments exposed in the Butana Bridge area. This study reports luminescence dates of 17 samples using both quartz and feldspar minerals, and establishes a detailed chronology of the Pleistocene fluvial sequence of the middle Atbara. The luminescence ages are also compared with radiocarbon (^{14}C) and ^{230}Th/U ages from fossil shells and bones, after applying screening criteria (Scholz and Mangini, 2007; Pasquetti et al., 2021).

2. Stratigraphy and samples

2.1. Stratigraphy

The sedimentary sequence in the Butana Bridge area (Al Sharafa and Al Shahateb on the west and east banks, respectively) was already described in detail by Abbate et al. (2010). On both banks of the Atbara the sedimentary sequence of about 40 m thick is exposed, indicating that the river started to incise after the deposition of KGS3. The sediments are subdivided by erosional unconformities and consist of fluvial sediments, including river channel deposits and floodplain sediments with palaeosols. Composite graphic logs of the sedimentary sequence at both Al Sharafa and Al Shahateb are shown in Fig. 2.

The lowest sedimentary unit, BBS, consists of three intervals (BBS1-3), which are particularly well developed in the Al Sharafa area on the western bank of the Atbara River. Here, channel fills of massive, horizontally or cross-bedded gravels form the basal interval (BBS1), with minor intercalations of fine-grained floodplain deposits. The sedimentary characteristics, along with the palaeocurrent directions inferred from the clast imbrications and the dip directions of the cross-beds, indicate unidirectional northward-flowing braided river channels with strongly fluctuating or highly seasonal runoff. The overlying interval BBS2 contains isolated gravelly channel fills at its base but consists predominantly of silty and fine sandy floodplain deposits with calcareous palaeosols. Compared to BBS1, these sedimentary features indicate decreasing river runoff, greater channel stability and the presence of

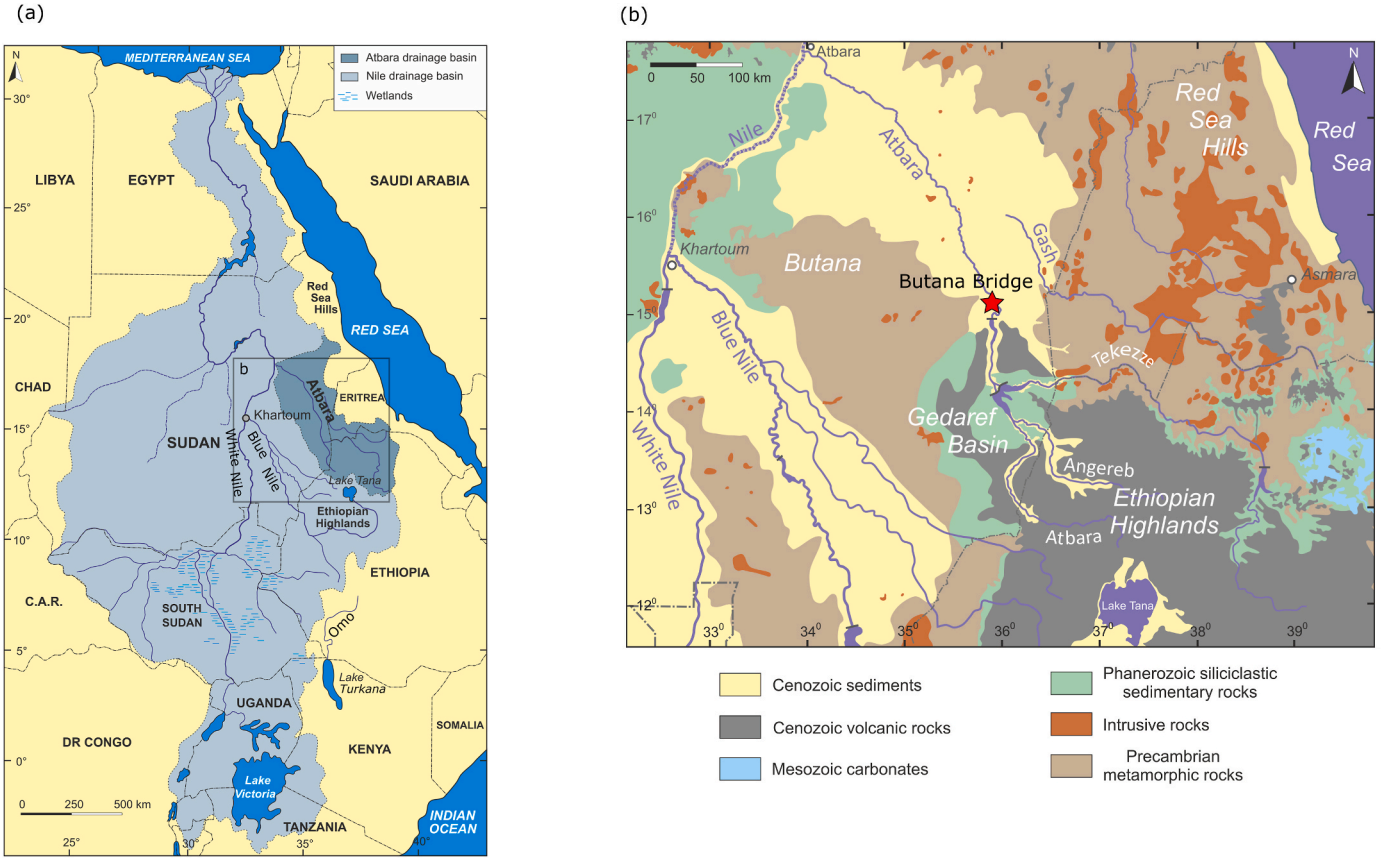

Fig. 1. Maps showing (a) the Atbara River drainage within the larger Nile Basin (modified after Williams, 2012), and (b) the geology of the study area. The star in (b) shows the location of the study area.

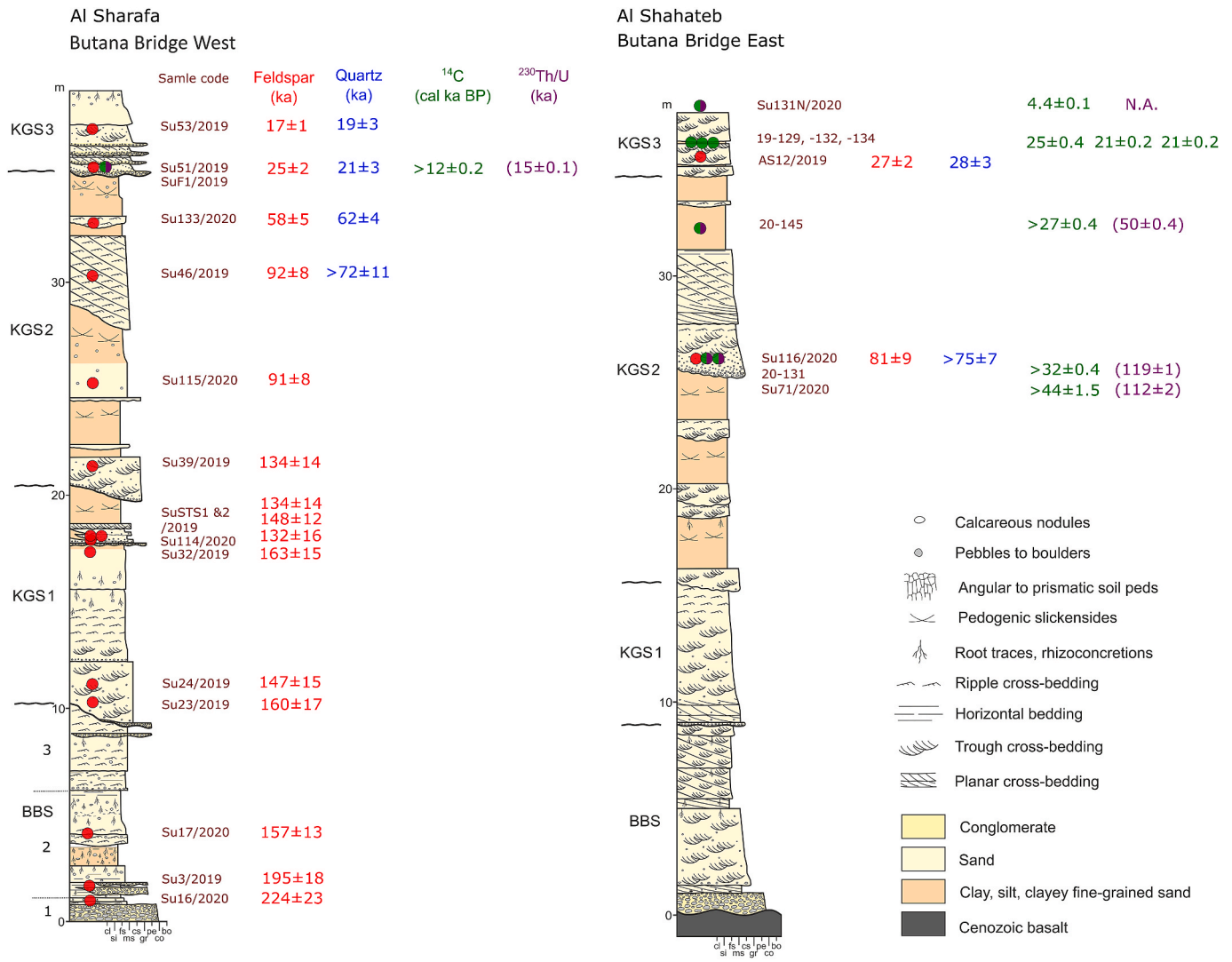

Fig. 2. Composite graphic logs of the middle Atbara fluvial sedimentary sequence as exposed at Al Sharafa and Al Shahateb, near the Butana Bridge. The stratigraphic position and age of the luminescence (red), ^{14}C (green) and ^{230}Th/U (purple) samples are also shown. Circles in half-green and half-purple are samples dated using both ^{14}C and ^{230}Th/U methods. The samples of ^{230}Th/U ages in parenthesis did not fullfil the screening criteria, and the ages were regarded as unreliable.

stable floodplains over longer periods in a dry climate. BBS3 consists mainly of fine sandy and silty ripple cross-bedded channel and floodplain sediments with isolated rhizoliths. These sediment characteristics show that the channel runoffs remained low. In contrast to the sediment sequence on the west bank of the Atbara River (Al Sharafa area), river channel deposits dominate in intervals BBS2 and BBS3 on the east bank (Al Shahateb area), while floodplain deposits are rare.

Unit KGS1 starts at the base with sandy-gravelly and predominantly trough cross-bedded river channel deposits cut deeply into the BBS, and which form fining-upward sequences and show lateral accretion surfaces. Higher in the unit, tabular to lenticular bodies of fine sands and muds are intercalated, often showing features of soil development. The sediment characteristics indicate that the sandy-gravelly sediments represent primarily subaqueous dune and point bar deposits of meandering rivers, whereas the fine-grained sediments represent floodplain and oxbow lake deposits, which were partly subjected to soil formation.

Unit KGS2 again begins at the base with sandy to gravelly and predominantly trough cross-bedded channel deposits, which are deeply incised into the underlying KGS1. The channel deposits are overlain by a sequence of laterally extensive fine sandy and silty sediments, into which numerous horizons with carbonate concretions and pedogenic slickensides are intercalated. Into the fine-grained sediments, isolated channel fills of mainly ripple cross-bedded fine sand and silt are intercalated, many of which show lateral accretion surfaces. In addition, the channels are bordered by laterally extensive 'wings', as already noted by Abbate et al. (2010). Mud lenses and rhizoliths often occur within the channel fills. Palaeocurrent directions are widely scattered, but the mean flow direction lies between north and west. Overall, the sediment characteristics indicate high-sinuosity meandering channels, although often rather strongly stabilised. Together with the palaeosols interpreted as fossil vertisols, this suggests a seasonal subhumid climate.

Unit KGS3 in the Al Sharafa area consists, at its base, of amalgamated lenticular to tabular sandy-gravelly sediment bodies, each of which is erosively bounded at its base, and which are generally overlain by massive fine sandy and carbonate-bearing sediments. In the Al Shahateb area, the KGS3 is predominantly built up of trough or ripple cross-bedded sands with rare lateral accretion surfaces of point bar origin. The channel deposits represent small stabilised channels of a braided and most probably highly seasonal or ephemeral fluvial system. However, widely scattered palaeocurrent directions and rare point bar deposits suggest that high-sinuosity channels were also present. In addition to the fluvial deposits, calcareous and weakly developed palaeosols also indicate a relatively arid climate.

2.2. Samples

A total of 17 samples for luminescence dating were taken from the Butana Bridge area; 15 from Al Sharafa and 2 from Al Shahateb (Table S1). The samples were collected by hammering opaque plastic cylinders into cleaned outcrop surfaces, except Su32/2019 which was collected at night by scraping sediment into a light-tight container. Samples for dose rate measurements were collected separately using sealed plastic bags and/or plastic containers. Additionally, 3 bone and 5 freshwater mollusc shell samples were collected for radiocarbon dating and the same 5 shell samples were also dated using the ^{230}Th/U method (Table S2). The stratigraphic positions of all samples are marked in Fig. 2.

3. Luminescence dating

3.1. Instrumentation

All luminescence measurements were performed using two Risø TL/OSL-20 automated readers equipped with both blue and infrared (IR) LEDs as stimulation light sources, as well as a calibrated ^{90}Sr/^{90}Y beta source. The reader was also equipped with a pulsed stimulation attachment, which enables the LEDs to be pulsed, and the signal to be detected during the off-time of the stimulation light (Lapp et al., 2009). The quartz optically stimulated luminescence (OSL) signal was stimulated with the blue LEDs (470 nm) and detected through a 7.5 mm Hoya U-340 filter. The feldspar infrared stimulated luminescence (IRSL) signal was measured by stimulating with the IR LEDs (870 nm) and detected through a combination of Schött 7–59 and BG39 filters, which transmits violet-blue luminescence signal between ~380 and 460 nm. The pulsed IR stimulation was performed with repetitive 100 μs on- and 400 μs off-time for 500 s, for a total on-time of 100 s. The pulsed IRSL signal was detected only during the off-time of the LED pulses, which started at 21.5 μs after the LEDs were switched off (Tsukamoto et al., 2017).

3.2. Luminescence sample preparation

The luminescence samples were sieved using sieves of 63, 100, 150, 200, 250 and 300 μm aperture sizes. For each sample, a grain size fraction that yielded the largest amount of material was selected for further pre-treatments. If a single sieved fraction did not yield enough material (less than ~5 g), two to three fractions were merged together. The selected grain size fraction for each sample is shown in Table S1. The sieved samples were treated with 10% hydrochloric acid, sodium oxalate, and 30% hydrogen peroxide to remove carbonate, aggregates and organic matter, respectively. Finally K-rich feldspar grains were separated using sodium polytungstate (SPT) solution between the densities of 2.54 and 2.58. The quartz rich fraction was separated between the densities of 2.62 and 2.70, and was etched by 40% HF for 1 h to extract quartz. Multigrain aliquots for luminescence measurements were made using 9.8 mm diameter stainless steel discs. Quartz and K-feldspar grains with ~2 or 6 mm diameter were mounted on discs using silicone oil as adhesive material.

3.3. Dose rate measurement

Samples were dried at 110 °C in an oven for 24 h. The dried sample materials of either 700 g or 50 g were sealed into a Marinelli beaker or a plastic container, and were used for the gamma spectrometry measurements. The samples were stored for at least four weeks to ensure equilibrium of ^{222}Rn. The gamma rays of the samples were detected using an Ortec pure Ge N-type gamma spectrometer. The activity of radionuclides was measured by gamma rays from ^{40}K for K, ^{214}Pb and ^{214}Bi for U, and ^{228}Ac, ^{208}Tl and ^{212}Pb for Th and converted to the concentration of K, U, and Th. The environmental dose rate for each sample was calculated using the dose rate conversion factors of Liritzis et al. (2013), beta attenuation factors by Guérin et al. (2012), and cosmic dose rate estimation following Prescott and Hutton (1994). The in-situ water content was used to calculate the effects of moisture on the dose rate. The mean burial depth was assumed from the sample position within the composite sediment profiles (Fig. 2), and the half depth considering ±50% uncertainty (Table S1) was used. The alpha efficiency and the internal K concentration for K-feldspar were assumed to be 0.09 ± 0.02 (Schmidt et al., 2018) and 12.5 ± 0.5% (Huntley and Baril, 1997). The dose rates are summarised in Table S1.

3.4. Quartz OSL dating

The six uppermost samples from KGS2 and KGS3 were used for quartz OSL dating. A standard single aliquot regenerative (SAR) dose protocol for quartz OSL was applied for the OSL equivalent dose (D_e) measurements (Murray and Wintle, 2000; Table S3a). To select a suitable heat treatment for the SAR protocol, a dose recovery test with different preheat temperatures was conducted using Su51/2019. Aliquots were bleached using the blue LEDs within a reader at room temperature for 300 s twice with the second bleach after a 10,000 s pause, then a beta dose of 35 Gy was given. This artificial dose was used as a surrogate natural dose. SAR protocols with preheat temperatures between 180 and 280 °C (10 s) with a cutheat of 20 °C lower than the preheat were applied to test the ability of the protocol to recover the given beta dose. The recovered to given dose ratio (dose recovery ratio) was all close to unity between 0.97 and 1.03 except the preheat at 280 °C with a ratio of 1.18. For the D_e measurements, a preheat temperature of 260 °C (10 s) was selected, which gave the best dose recovery ratio of 0.99 ± 0.02. The OSL signal intensity was calculated using the first 1 s of the OSL signal minus the early background of the following 3 s. Between 16 and 24 aliquots for each sample were measured for the determination of D_e and the mean value (±1σ standard error) was calculated. All aliquots showing the recycling ratio and OSL IR depletion ratio (Duller, 2003) outside ± 10% from unity was rejected.

The natural OSL signal of Su46/2019 and Su116/2020 (from KGS2) was found to be close to the signal saturation level of the laboratory dose response curve. For each measured aliquot of these samples, the calculated D_e value was compared with 2 times characteristic saturation dose (D_0) of the fitted dose response curve. For ten aliquots out of sixteen in both samples, the D_e value was larger than $2D_0$. We therefore conclude that the natural quartz OSL of these two samples was indistinguishable from saturation, and a minimum age was given by the $2D_0$ divided by the dose rate. The quartz OSL ages are listed in Table 1.

3.5. Feldspar IRSL dating

To select the most suitable feldspar luminescence signal in this study, the sample As12/2019 was measured with multiple signals and compared to the quartz OSL age. The two commonly applied post-IR IRSL protocols, with elevated temperature IRSL simulations at 225 °C (termed $pIRIR_{225}$; Thomsen et al., 2008; Buylaert et al., 2009) and at 290 °C ($pIRIR_{290}$; Thiel et al., 2011) were used, as well as the pulsed IRSL signal at 50 °C (pulsed IR_{50}; Tsukamoto et al., 2017). The pIRIR signal has been known to reduce anomalous fading, but the signal is more difficult to bleach than the low temperature IRSL signal typically measured at 50 °C (IR_{50}). Tsukamoto et al. (2017) showed that the pulsed IR_{50} signal is as bleachable as the continuous wave IR_{50} and also as stable as the pIRIR. The protocols are shown in Table S3b-d. For all three protocols, a test of anomalous (athermal) fading was also conducted using the method following Auclair et al. (2003). The fading rate (g_{2days}-value) was determined, and both fading uncorrected and corrected ages were calculated using the method of Huntley and Lamothe (2001). The result indicates that only the fading corrected pulsed IRSL signal agrees with the quartz OSL age (Fig. 3), whereas the fading corrected $pIRIR_{225}$ and $pIRIR_{290}$ ages overestimated the quartz age by 46 and 54%, respectively. Although we currently have no firm evidence of

Table 1
Equivalent doses and ages.

Sample	Quartz D_e (Gy)	Quartz age (ka)	Feldspar D_e (Gy)	g_{2days}-value (%/decade)	Recombination centre density	Fading uncorrected age (ka)	Fading corrected age (ka)
Al Sharafa							
Su53/2019	22 ± 3	19 ± 3	25.7 ± 1.4	2.7 ± 0.3	1.9E-06 ± 1.6E-07	14 ± 1	17 ± 1
Su51/2019	23 ± 3	21 ± 3	40.1 ± 5.1	2.6 ± 0.2	1.7E-06 ± 1.7E-07	20 ± 2	25 ± 2
Su133/2020	91 ± 3	62 ± 4	98.3 ± 2.0	1.3 ± 0.3	9.1E-07 ± 2.1E-07	44 ± 4	58 ± 5
Su46/2019	>122 ± 18	>72 ± 11	131 ± 5	3.1 ± 0.3	2.1E-06 ± 1.7E-07	56 ± 5	92 ± 8
Su115/2020			130 ± 5	2.3 ± 0.3	1.5E-06 ± 2.0E-07	62 ± 6	91 ± 8
Su39/2019			265 ± 9	1.9 ± 0.3	1.4E-06 ± 2.2E-07	92 ± 10	134 ± 14
SuSTS1/2019			268 ± 10	2.4 ± 0.3	1.6E-06 ± 2.0E-07	86 ± 9	134 ± 14
SuSTS2/2019			186 ± 4	2.7 ± 0.3	1.9E-06 ± 2.1E-07	89 ± 7	148 ± 12
Su114/2020			243 ± 8	2.7 ± 0.3	1.8E-06 ± 1.8E-07	82 ± 10	132 ± 16
Su32/2019			210 ± 6	2.7 ± 0.3	1.9E-06 ± 1.7E-07	99 ± 9	163 ± 15
Su24/2019			277 ± 10	2.2 ± 0.3	1.5E-06 ± 2.2E-07	96 ± 10	147 ± 15
Su23/2019			291 ± 12	2.5 ± 0.3	1.7E-06 ± 1.7E-07	98 ± 10	160 ± 17
Su17/2020			192 ± 5	3.1 ± 0.3	2.1E-06 ± 2.1E-07	87 ± 7	157 ± 13
Su3/2019			246 ± 10	2.9 ± 0.3	2.0E-06 ± 2.1E-07	112 ± 10	195 ± 18
Su16/2020			249 ± 14	3.0 ± 0.3	2.0E-06 ± 2.2E-07	126 ± 13	224 ± 23
Al Shahateb							
AS12/2019	53 ± 5	28 ± 3	54.6 ± 1.5	2.3 ± 0.3	1.5E-06 ± 1.7E-07	22 ± 1	27 ± 2
Su116/2020	>112 ± 7	>75 ± 7	124 ± 3	2.0 ± 0.3	1.4E-06 ± 2.0E-07	57 ± 6	81 ± 9

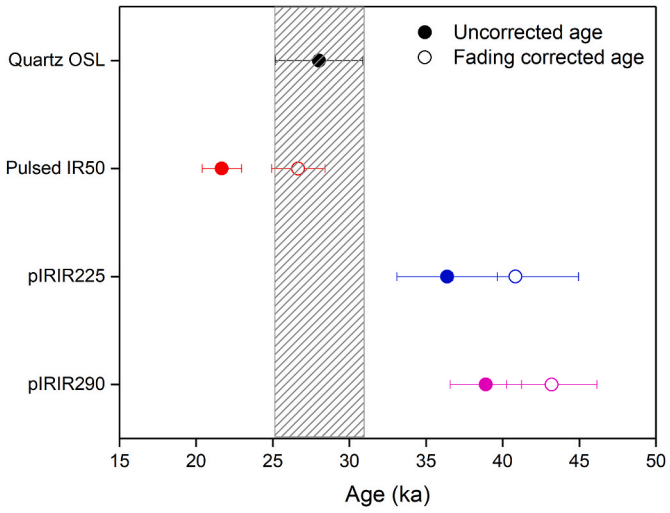

Fig. 3. Comparison of quartz OSL, feldspar $pIRIR_{225}$ and $pIRIR_{290}$, and pulsed IR_{50} ages of AS12/2019.

the cause of the overestimation of the $pIRIR_{225}$ and $pIRIR_{290}$ ages, a plausible explanation is incomplete resetting of the pIRIR signal before deposition, since the pIRIR signal needs much longer time to be bleached compared to the low temperature IR_{50} signal (Colarossi et al., 2015; Tsukamoto et al., 2017).

For relatively young samples (<30 ka) used by Tsukamoto et al. (2017), all measurement performances of the pulsed IR_{50} signal (with a preheat of 250 °C for 60 s) were satisfactory. However for older samples, a poor dose recovery ratio of ~0.80 was reported (Li et al., 2018). We therefore compared the performance of the pulsed IR_{50} protocol in terms of anomalous fading rate and the dose recovery ratio, applying different preheat temperatures between 230 and 290 °C with 20 °C increments (60s) for Su39/2019. For the dose recovery test, aliquots were bleached using a solar simulator (Hönle SOL2) for 4 h. A beta dose of 246 Gy was given for all aliquots and the pulsed IR_{50} protocol was used to measure the applied dose. Three aliquots for each preheat temperature were used. A fading test was also conducted using the same set of preheat temperatures using six aliquots. The results are shown in Fig. 4a and b. The dose recovery ratios fell in the range of ~0.9–1.0 for all temperatures, with a tendency of increasing ratio with the temperature. However, the fading rate also slightly increased with the preheat temperature with the g_{2days}-values from 1.95 ± 0.18% for 230 °C to 2.32 ± 0.09% at 270 °C and 2.29 ± 0.13% at 290 °C. We selected the preheat temperature of 230 °C for the pulsed IR_{50} protocol, because of the lower fading rate and acceptable dose recovery ratio.

The signal intensity of the pulsed IR_{50} was calculated by the initial 20 s of the signal minus the last 30 s (the initial 4 s and the last 6 s of the LED on-time). The dose recovery test for the applied pulsed IR_{50} protocol was also conducted for all samples, and the mean dose recovery ratio was 0.92 ± 0.01, which is in the acceptable range (Fig. 4c). A fading test was conducted for all samples, and the g_{2days}-value as well as the recombination centre density (Huntley, 2006) was calculated.

Twelve aliquots per sample were used for the D_e measurements. The D_e values and fading uncorrected ages of three young samples from KGS3 (Su51/2019, Su53/2019 and AS12/2019) were calculated using the arithmetic mean of 12 aliquots obtained from the standard SAR procedure. The ages were fading-corrected following Huntley and Lamothe (2001), because the natural pulsed IR_{50} of these samples are still in quasi-linear part of the dose response curve. For all the other samples, three aliquots for each sample were used to construct the full dose response curve, and the remaining aliquots were measured only for the natural signal and a test dose signal (L_n and T_n). A standardised dose response curve for each sample was used to calculate the unfaded and simulated natural dose response curves for the fading correction method of Kars et al. (2008) using the R Luminescence Package. D_e values, fading uncorrected and corrected ages are summarised in Table 1.

4. Radiocarbon and ^{230}Th/U dating

Radiocarbon dating of all 8 samples (3 bone, 5 freshwater molluscs) was performed at the Leibniz-Laboratory for Radiometric Dating and Stable Isotope Research, Kiel, Germany, using the type HVE 3 MV Tandetron 4130 accelerator mass spectrometer (AMS). Since the bone samples (19–129, 19–132, 19–134) did not contain collagen, the measurement was conducted on the carbon fraction of the bioapatite, after removing contaminated calcite using acetic acid. ^{14}C age, δ^{13}C, and calibrated ^{14}C ages using Intcal20 (Reimer et al., 2020) are summarised in Table S4.

^{230}Th/U dating of the same 5 shell samples was carried out by Isobar Science, using Thermo Fisher Neptune PlusTM multi-collector inductively coupled plasma mass spectrometry (MC-ICP-MS), and the data are

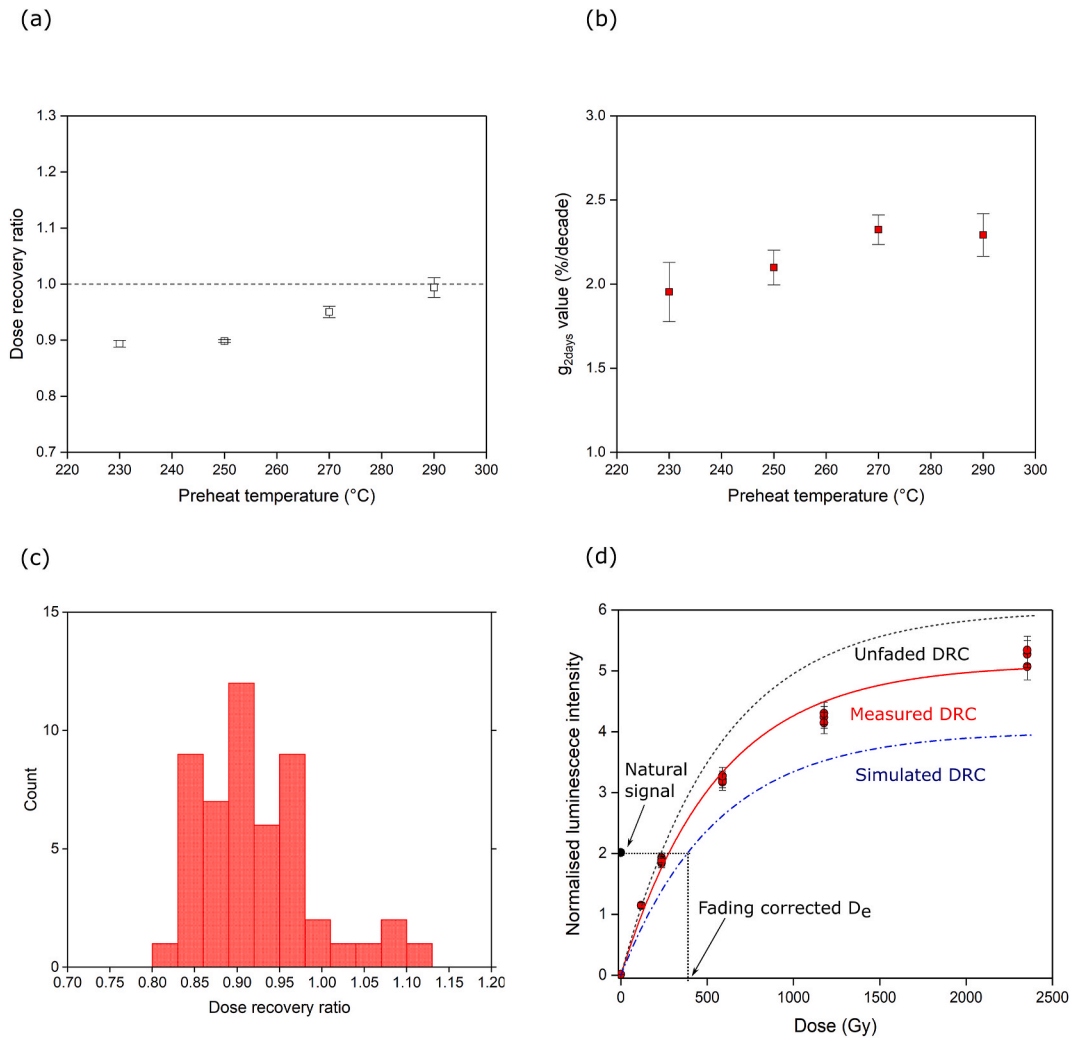

Fig. 4. Pulsed IR_{50} signal characteristics. (a) Dose recovery ratio and (b) fading rate of Su39/2019 at different preheat temperatures, (c) dose recovery ratio of all samples, and (d) fading correction of Su39/2019.

shown in Table S5. The aragonite/calcite ratio of the shell samples was determined by X-ray diffractometry at Technische Üniversität Berlin (Table S4 and S5).

5. Chronology results

For the uppermost part of the Al Sharafa and Al Shahateb sections, where both quartz OSL and fading corrected K-feldspar pulsed IR_{50} ages were obtained, the ages from the two minerals are in good agreement (Table 1, Fig. 2). Since the bleachability of the IR_{50} signal is more than an order of magnitude slower than the quartz OSL signal (e.g. Godfrey-Smith et al., 1988; Murray et al., 2009), the agreement indicates that both signals were well bleached before burial and the ages are reliable. The quartz OSL signal, however, reached saturation at ~70 ka (~120 Gy). We therefore relied on the fading-corrected pulsed IR_{50} ages (Table 1, Fig. 2) to determine the chronology of the Pleistocene middle Atbara sediments.

The shell samples dated using ^{14}C and $^{230}Th/U$ methods were originally aragonite but contained varying amounts of calcite due to diagenesis (1–78%, Tables S4 and S5). Diagenesis of aragonite to calcite can significantly affect both ^{14}C and $^{230}Th/U$ ages, therefore a selection of reliable results is necessary. Scholz and Mangini (2007) listed several screening criteria for corals for $^{230}Th/U$ dating, and two of these could be applied to freshwater aragonitic shells: 1) ^{232}Th concentration lower than 2 ppb, and 2) calcite content lower than 2%. More recently, Pasquetti et al. (2021) developed criteria for selecting reliable ages from large numbers of published $^{230}Th/U$ data from the Mediterranean Sea, and those applicable to aragonitic shells were: 1) calcite content lower than 3%, 2) ^{238}U concentration of less than 1%, and 3) $^{230}Th/^{232}Th$ activity ratio larger than 40. None of our dated shell samples fulfils these criteria and the ages could not be considered as reliable (Table S5).

We also applied the criterion of the calcite content for shells for ^{14}C dating, because when aragonite is recrystalized to calcite, carbon atoms should be replaced by modern carbon. Only the sample Su 131N/2020 has less than 3% calcite content, and therefore the ^{14}C age of this sample should be reliable. We regard other ^{14}C dates from shells as minimum ages.

The remaining 3 samples (19–129, 19–132, 19–134) for ^{14}C dating are fossil bones. Cherkinsky (2009) and Zasso and Saliège (2011) suggested that bioapatite could be a suitable material for ^{14}C dating. They compared ^{14}C ages obtained from different materials from the same bone samples (collagen, bioapatite of calcined and non-calcined bones) and found that these were generally in agreement for samples from Africa and the Arabian Peninsula in arid environments. We therefore regard the bone ^{14}C ages as reliable, although there are no established quality assessment criteria for bioapatite. All luminescence, ^{14}C and $^{230}Th/U$ ages from Al Shahateb are plotted in Fig. S1. The selected and rejected ages according to the screening are shown in filled and open symbols, respectively. The selected ages are internally and stratigraphically consistent, whereas the rejected ages are widely scattered,

indicating the validity of the screening, as well as the reliability of the selected dataset.

The pulsed IR_{50} ages of samples from BBS intervals 1 and 2 indicate an age of 224 ± 23 to younger than 157 ± 13 ka, corresponding to MIS7 and MIS6. The pulsed IR_{50} ages of all 6 samples from KGS1 show high overlap, and are consistent with a range from 163 ± 15 to 132 ± 16 ka, corresponding to MIS6. According to our luminescence chronology therefore, there is no significant age gap between the KGS and BBS synthems, contrary to the findings of Abbate et al. (2010).

The age of the KGS2 spanned from 134 ± 14 ka to younger than 58 ± 5 ka, as determined by four samples from the Al Sharafa section. The age of Su116/2020 from a channel about midway in the KGS2 at Al Shahateb is 81 ± 8 ka, which is also consistent with two samples in the Al Sharafa section from a similar depth (91 ± 8 ka). The depositional period of KGS2 therefore corresponds to MIS5 to MIS4 or 3. The ^{230}Th/U age of a shell at the bottom of KGS2 (126 ± 1ka) by Abbate et al. (2010) is consistent with our pulsed IR_{50} age of Su39/2019 (134 ± 14 ka), though we are unable to fully assess whether this sample passes our screening criteria.

The pulsed IR_{50} ages as well as three bone ^{14}C ages from KGS3 indicate that this unit spans from 27 ± 2 ka to younger than 17 ± 1 ka and can therefore be correlated to MIS2. This is in contrast to the results of Abbate et al. (2010), who correlated the base of the KGS3 to MIS5c using a ^{230}Th/U age of 92.2 ± 0.7 ka. However, this sample does not fullfil our streening criteria, because the ^{238}U concentration exceeds 1% (Table 5 of Abbate et al., 2010). The shell sample Su131N/2020 was collected from a surface scatter that included shells, lithics, and ceramics, located high up on KGS3 sediments at Al Shahateb. Its ^{14}C age (4.4 ± 0.1 cal ka BP, Table S4) suggests this assemblage may correspond to the Holocene occupations described from this region by Marks (1987). Since this was a surface find, however, the exact relationship to the rest of the sequence is unclear.

6. Discussion

The mean palaeocurrent directions derived from the palaeocurrent indicators in the BBS and KGS suggest that the headwaters of the rivers were predominantly located in the south and east, i.e. in what is now the northern Ethiopian highlands and Eritrea (Fig. 1a). Therefore, we discuss the chronology of the fluvial sedimentation of the BBS and KGS in view of the climate of the headwater area, and compare with the chronologies of the Blue Nile, as well as with that of the Omo River, in southern Ethiopia, since the Atbara, Blue Nile and Omo share a common watershed divide near Lake Tana (Fig. 1a).

Precipitation in the Ethiopian highlands is dominated by the summer monsoon, when the Intertropical Convergence Zone (ITCZ) shifts northwards in boreal summer. Intensified monsoonal precipitation over East Africa leads to high Nile runoff into the eastern Mediterranean, resulting in the deposition of organic-rich muds, called sapropels (Rossignol-Strick et al., 1982). Occurrences of Mediterranean sapropel units over the last ~240 ka (S9 to S1) are believed to have coincided with insolation maxima in the northern hemisphere (Rossignol-Strick, 1983). (Ages and numbers of the sapropel units follow Lourens et al. (1996).) More recently, insolation maxima were shown to also match with the precipitation index (leaf wax hydrogen isotopes) from Chew Bahir lake, and that these were mainly controlled by orbital precession at a 21 kyr cycle (Lupien et al., 2022).

The correlation between Nile flooding and Mediterranean sapropel formation was further confirmed by a chronology of extreme flooding episodes along the Nile River, and which were synchronous with sapropel units S5 (~124 ka) to S1 (~8 ka, Williams et al., 2015). A temporal correlation between flood sediments and older sapropel units — S9 (~240 ka) to S6 (~172 ka) — was less clear, but this was due to the larger uncertainty of the quartz OSL dating (Williams et al., 2015).

The Middle to Late Pleistocene sediments of the Omo River, i.e. the Kibish Formation, have been studied extensively and have produced

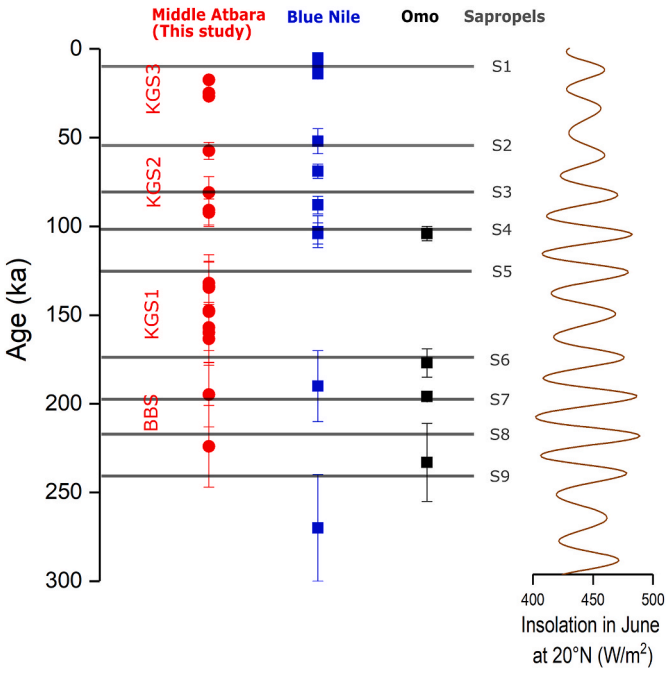

Fig. 5. Comparison of pulsed IR_{50} ages from the Middle Atbara, quartz OSL ages from the Blue Nile channels (Williams et al., 2015), ^{40}Ar/^{39}Ar ages of intercalated tephras in the Kibish Formation (Omo River, McDougall et al., 2005; 2008) and the timing of eastern Meditranian sapropels (Lourens et al., 1996; Vidal et al., 2022). Oscillations of the low latitude insolation in summer (June) is also shown (Lasker et al., 2004).

important fossils of early *Homo sapiens*, namely the crania Omo I and Omo II. The Kibish Formation was divided into 4 Members (from bottom to top, I-IV). Members I and III were dated to ~196 and ~104 ka, respectively, based on ^{40}Ar/^{39}Ar dating of tuffs within them, and these were then correlated to sapropel units S7 (~195 ka) and S4 (~102 ka), respectively (McDougall et al., 2005; 2008). However, this correlation was recently questioned by the dating of a tuff in Member II to 233 ± 22 ka, indicating that Member I must be older, and shedding doubt on the proposed correlation of Kibish Member deposition with Mediterranean sapropel units (Vidal et al., 2022).

Due to the relatively large uncertainty of the fading corrected pulsed IR_{50} ages of the middle Atbara sediments, one-to-one correlation between individual sapropel units and higher energy deposits of the BBS and KGS is difficult. Nevertheless, the ages of the higher energy beds the BBS, KGS1 and KGS2 are broadly consistent with precession cycles, and with the ages of S9 to S2 (Fig. 5). It is also interesting to note that the age range of the eastern Mediterranean sapropels (S9 – S1), high-energy fluvial sediments deposited under humid climate of the Middle Atbara, Nile and Omo rivers are similar, starting from ~240 ka. The deposition of these sediments may be triggered by a climatic shift in their catchments with an increase in runoff. This period coincides with increased amplitude of low latitude insolation (Lupien et al., 2022).

7. Summary

New luminescence ages suggest the entire BBS and KGS sequence exposed along the middle Atbara River was deposited between 224 ± 23 ka and <17 ± 1 ka. For the KGS3, the quartz and feldspar pulsed IR_{50} ages showed excellent agreement, confirming the reliability of the applied protocol. The luminescence age of each unit was determined as ~220–160 ka (BBS), ~160–130 ka (KGS1), ~130–60 ka (KGS2), and ~30 - <17 ka (KGS3), indicating a continuous sequence of deposition through the late Middle and Late Pleistocene, with episodes of high-energy deposition possibly correlated with periods of high Nile

discharge and sapropel formation in the Mediterranean.

Our results significantly revise the chronology of the middle Atbara River Valley. We confirm Abbate's et al.'s (2010) interpretation for the relatively young age (i.e. <200 ka) of Acheulean assemblages in the KGS1. In contrast to these authors, we find that the underlying BBS is entirely late Middle Pleistocene in age, and that no major time unconformity exists between it and the overlying KGS. Additionally, we find that the KGS 2 and KGS 3 span a much longer interval than previously proposed, from ~130 ka to younger than 17 ka. The sedimentary sequences of the middle Atbara therefore have high potential for the reconstruction of archaeological and faunal dynamics in the middle Nile Basin over the last 200 kyr.

Declaration of competing interest

The authors declare that they have no known competing financial interests or personal relationships that could have appeared to influence the work reported in this paper.

Acknowledgements

This work was supported by the German Research Foundation (Deutsche Forschungsgemeinschaft, DFG, grant no. 387794796 to F.B. and S.T.) and a National Geographic Exploration grant (no. CP-086R-17 to F.B.). We thank the Geological Research Authority of Sudan for sample export permissions. Sabine Mogwitz, Petra Posimowski and Gwynlyn Buchanan are thanked for luminescence sample preparations and gamma spectrometry measurements. Denis Scholz and Christian Zeeden are thanked for discussion. Mudather Ahmed, Hamed Basher, Mohammed Bedri, Aisha Huseen, Osman Khalil, Xavier Muth, Sakir Önder Özkurt, Marten Schöle, Thomas Schossleitner, Manal Siyam, and Aisha Wali-Sayed assisted in fieldwork. Constructive comments from the reviewer and the guest editor improved the paper significantly.

Appendix A. Supplementary data

Supplementary data related to this article can be found at https://doi.org/10.1016/j.quageo.2022.101312.

References

Abbate, E., Albianelli, A., Awad, A., Billi, P., Bruni, P., Delfino, M., Ferretti, M.P., Filippi, O., Gallai, G., Ghinassi, M., Lauritzen, S.E., Lo Vetro, D., Martinez-Navarro, B., Martini, F., Napoleone, G., Bedri, O., Papini, M., Rook, L., Sagri, M., 2010. Pleistocene environments and human presence in the middle Atbara valley (Khashm El Girba, eastern Sudan). Palaeogeogr. Palaeoclimatol. Palaeoecol. 292, 12–34.

Arkell, A.J., 1949. The old stone age in the Anglo-Egyptian Sudan. Sudan Antiq. Serv. Occas. Pap. 1, 1–52.

Auclair, M., Lamothe, M., Huot, S., 2003. Measurement of anomalous fading for feldspar IRSL using SAR. Radiat. Meas. 37, 487–492.

Buylaert, J.P., Murray, A.S., Thomson, K.J., Jain, M., 2009. Testing the potential of an elevated temperature IRSL signal from K-feldspar. Radiat. Meas. 44, 560–565.

Cherkinsky, A., 2009. Can we get a good radiocarbon age from "bad bone"? Determining the reliability of radiocarbon age from bioapatite. Radiocarbon 51, 647–655.

Clark, J.D., Beyene, Y., WoldeGabriel, G., Hart, W.K., Renne, P.R., Gilbert, H., Defleur, A., Suwa, G., Katoh, S., Ludwig, K.R., Boisserie, J.-R., Asfaw, B., White, T.D., 2003. Stratigraphic, chronological and behavioural contexts of Pleistocene Homo sapiens from middle Awash, Ethiopia. Nature 423, 747–752.

Colarossi, D., Duller, G.A.T., Roberts, H.M., Tooth, S., Lyons, R., 2015. Comparison of paired quartz OSL and feldspar post-IR IRSL dose distributions in poorly bleached fluvial sediments from South Africa. Quat. Geochronol. 30, 233–238.

Duller, G.A.T., 2003. Distinguishing quartz and feldspar in single grain luminescence measurements. Radiat. Meas. 37, 161–165.

Godfrey-Smith, D.I., Huntley, D.J., Chen, W.H., 1988. Optical dating studies of quartz and feldspar sediment extracts. Quat. Sci. Rev. 7, 373–380.

Guérin, G., Mercier, N., Nathan, R., Adamiec, G., Lefrais, Y., 2012. On the use of the infinite matrix assumption and associated concepts: a critical review. Radiat. Meas. 47, 778–785.

Huntley, D.J., 2006. An explanation of the power-law decay of luminescence. J. Phys. Condens. Matter 18, 1359–1365.

Huntley, D.J., Baril, M.R., 1997. The K content of the K-feldspars being measured in optical dating or in thermoluminescence dating. Ancient TL 15, 11–13.

Huntley, D.J., Lamothe, M., 2001. Ubiquity of anomalous fading in K-feldspars and the measurement and correction for it in optical dating. Can. J. Earth Sci. 38, 1093–1106.

Kars, R.H., Wallinga, J., Cohen, K.M., 2008. A new approach towards anomalous fading correction for feldspar IRSL dating — tests on samples in field saturation. Radiat. Meas. 43, 786–790.

Lapp, T., Jain, M., Ankjærgaard, C., Pirzel, L., 2009. Development of pulsed stimulation and photon timer attachments to the Risø TL/OSL reader. Radiat. Meas. 44, 571–575.

Lasker, J., Robutel, P., Joutel, F., Gastineau, M., Correia, A.C.M., Levrard, B., 2004. A long-term numerical solution for the insolation quantities of the Earth. Astron. Astrophys. 428, 261–285.

Li, Y., Tsukamoto, S., Long, H., Zhang, J., Yang, L., He, Z., Frechen, M., 2018. Testing the reliability of fading correction methods for feldspar IRSL dating: a comparison between natural and simulated-natural dose response curves. Radiat. Meas. 120, 228–233.

Liritzis, I., Stamoulis, K., Papachristodoulou, C., Ioannides, K., 2013. A re-evaluation of radiation dose-rate conversion factors. Mediterr. Archaeol. Archaeom. 13, 1–15.

Lisiecki, L.E., Raymo, M., 2005. A Pliocene-Pleistocene stack of 57 globally distributed benthic $\delta^{18}O$ records. Paleoceanogr. Paleoclimatol. 20, PA1003.

Lourens, L.J., Antonarakou, A., Hilgen, F.J., Van Hoof, A.A.M., Vergnaud-Grazzini, C., Zachariasse, W.J., 1996. Evaluation of the Plio-Pleistocene astronomical timescale. Paleoceanography 11, 391–413.

Lupien, R., Russel, J.M., Pearson, E.J., Castañeda, I.S., Asrat, A., Foerster, V., Lamb, H.F., Roberts, H.M., Schäbitz, F., Trauth, M.H., Beck, C., Feibel, C.S., Cohen, A.S., 2022. Orbital controls on eastern African hydroclimate in the Pleistocene. Sci. Rep. 12, 3170.

Marks, A.E., 1987. Terminal Pleistocene and Holocene hunters and gatherers in the eastern Sudan. Anthony Afr. Archaeol. Rev. 5, 79–92.

McDougall, I., Brown, F.H., Fleagle, J.G., 2005. Stratigraphic placement and age of modern humans from Kibish, Ethiopia. Nature 433, 733–736.

McDougall, I., Brown, F.H., Fleagle, J.G., 2008. Sapropels and the age of hominins Omo I and II, Kibish, Ethiopia. J. Hum. Evol. 55, 409–420.

Murray, A.S., Wintle, A.G., 2000. Luminescence dating of quartz using an improved single-aliquot regenerative-dose protocol. Radiat. Meas. 32, 57–73.

Murray, A.S., Buylaert, J.P., Thomsen, K.J., Jain, M., 2009. The effect of preheating on the IRSL signal from feldspar. Radiat. Meas. 44, 554–559.

Pasquetti, F., Bini, M., Giaccio, B., Ratti, A., Vacchi, M., Zanchetta, G., 2021. Chronology of the Mediterranean sea-level highstand during the Last Interglacial: a critical review of the U/Th-dated deposits. J. Quat. Sci. 36, 1174–1189.

Potts, R., Behrensmeyer, A.K., Faith, J.T., Tryon, C.A., Brooks, A.S., Yellen, J.E., Deino, A. L., Kinyanjui, R., Clark, J.B., Haradon, C., Levin, N.E., Meijer, H.J.M., Veatch, E.G., Owen, R.B., Renaut, R.W., 2018. Environmental dynamics during the onset of the middle stone age in eastern Africa. Science 360 (6384), eaao2200.

Prescott, J.R., Hutton, J.T., 1994. Cosmic ray contributions to dose rates for luminescence and ESR dating: large depths and long-term time variations. Radiat. Meas. 23, 497–500.

Reimer, P., Austin, W., Bard, E., Bayliss, A., Blackwell, P., Bronk Ramsey, C., Butzin, M., Cheng, H., Edwards, R., Friedrich, M., Grootes, P., Guilderson, T., Hajdas, I., Heaton, T., Hogg, A., Hughen, K., Kromer, B., Manning, S., Muscheler, R., Palmer, J., Pearson, C., van der Plicht, J., Reimer, R., Richards, D., Scott, E., Southon, J., Turney, C., Wacker, L., Adolphi, F., Büntgen, U., Capano, M., Fahrni, S., Fogtmann-Schulz, A., Friedrich, R., Köhler, P., Kudsk, S., Miyake, F., Olsen, J., Reinig, F., Sakamoto, M., Sookdeo, A., Talamo, S., 2020. The IntCal20 Northern Hemisphere radiocarbon age calibration curve (0–55 cal kBP). Radiocarbon 62, 725–757.

Rossignol-Strick, M., 1983. African monsoons, an immediate climate response to orbital insolation. Nature 304, 46–49.

Rossignol-Strick, M., Nesteroff, W., Olive, P., Vergnaud-Grazzini, C., 1982. After the deluge: Mediterranean stagnation and sapropel formation. Nature 295, 105–110.

Schmidt, C., Bösken, J., Kolb, T., 2018. Is there a common alpha-efficiency in polymineral samples measured by various infrared stimulated luminescence protocols? Geochronometria 45, 160–172.

Scholz, D., Mangini, A., 2007. How precise are U-series coral ages? Geochem. Cosmochem. Acta 1935–1948.

Thiel, C., Buylaert, J.P., Murray, A., Terhorst, B., Hofer, I., Tsukamoto, S., Frechen, M., 2011. Luminescence dating of the Stratzing loess profile (Austria) – testing the potential of an elevated temperature post-IR IRSL protocol. Quat. Int. 234, 23–31.

Thomsen, K.J., Murray, A.S., Jain, M., Bøtter-Jensen, L., 2008. Laboratory fading rates of various luminescence signals from feldspar-rich sediment extracts. Radiat. Meas. 43, 1474–1486.

Tsukamoto, S., Kondo, R., Lauer, T., Jain, M., 2017. Pulsed IRSL: a stable and fast bleaching luminescence signal from feldspar for dating Quaternary sediments. Quat. Geochronol. 41, 26–36.

Vidal, C., Lane, C.S., Asrat, A., Barfod, D.N., Mark, D.F., Tomlinson, E.L., Tadesse, A.Z., Yirgu, G., Deino, A., Hutchison, W., Mounier, A., Oppenheimer, C., 2022. Age of the oldest known Homo Sapiens from eastern Africa. Nature 61, 579–583.

Williams, M., 2012. River sediments. Phil. Trans. R. Soc. A 370, 2093–2122.

Williams, M.A.J., Duller, G.A.T., Williams, F.M., Woodward, J.C., Macklin, M.G., El Tom, O.A.M., Munro, R.N., El Hajaz, Y., Barrows, T.T., 2015. Causal links between Nile floods and eastern Mediterranean sapropel formation during the past 125 kyr confirmed by OSL and radiocarbon dating of Blue and White Nile sediments. Quat. Sci. Rev. 130, 89–108.

Zasso, A., Saliège, J.-F., 2011. Radiocarbon dating of biological apatites: a review. Palaeogeogr. Palaeoclimatol. Palaeoecol. 310, 52–61.